NANO: Brief Reports and Reviews
Vol. 13, No. 11 (2018) 1850135 (8 pages)

DOI: 10.1142/S1793292018501357

MoS_2 Layers Decorated RGO Composite Prepared by a One-Step High-Temperature Solvothermal Method as Anode for Lithium-Ion Batteries

Xuehua Liu*,†, Bingning Wang*,†, Jine Liu*,†, Zhen Kong*,†, Binghui Xu*,†, Yiqian Wang‡ and Hongliang Li*,†,§

*Institute of Materials for Energy and Environment
Qingdao University, Qingdao 266071, P. R. China

†College of Materials Science and Engineering
Qingdao University, Qingdao 266071, P. R. China

‡College of Physics, Qingdao University
No. 308 Ningxia Road, Qingdao 266071, P. R. China
§lhl@qdu.edu.cn; lhlfap@163.com

Received 28 July 2018
Accepted 22 October 2018
Published 21 November 2018

A one-step high-temperature solvothermal approach to the synthesis of monolayer or bilayer MoS_2 anchored onto reduced graphene oxide (RGO) sheet (denoted as MoS_2/RGO) is described. It was found that single-layered or double-layered MoS_2 were synthesized directly without an extra exfoliation step and well dispersed on the surface of crumpled RGO sheets with random orientation. The prepared MoS_2/RGO composites delivered a high reversible capacity of 900 mAhg^{-1} after 200 cycles at a current density of 200 mAg^{-1} as well as good rate capability as anode active material for lithium ion batteries. This one-step high-temperature hydrothermal strategy provides a simple, cost-effective and eco-friendly way to the fabrication of exfoliated MoS_2 layers deposited onto RGO sheets.

Keywords: MoS_2 monolayer; RGO; solvothermal method; lithium-ion batteries.

1. Introduction

With the rapid development of the hybrid electric vehicles and other portable electronic devices, there is a growing demand for advanced energy storage and conversion technologies.[1–4] Lithium ion batteries (LIBs), as one of the most successful energy storage devices, have been attracting increasing interest due to the merits including high energy density, long cycle life, low self-discharge, environmental friendly nature and no memory effect.[5–7] The conventional graphite anode with a theoretical capacity of 372 mAh g^{-1} cannot fulfill the demand for high capacity LIBs.

As one of the typical graphite-like dichalcogenides, molybdenum disulfide (MoS_2) has been considered as promising anode material for LIBs. MoS_2 possesses many unique physical and chemical advantages originating from its layered structure: MoS_2 has a sandwich-like structure in which the Mo layers are clamped by two S layers, and the internal

§Corresponding author.

layers are connected by strong covalent bond (Mo–S) while the adjacent layers are joint together by weak van der Waals force. Therefore, lithium ions can easily intercalate into the gaps between layers without large volume expansion. The theoretical capability of MoS_2 is 670 mAh g^{-1} which is much higher than the commercial graphite anode. However, the pure MoS_2 anode suffers a lot from the poor rate capability and cycling stability because of the intrinsic low electric conductivity, the destruction of structure with the lithium ions successively intercalated/extracted progress and the generation of polysulfides Li_2S_x $(2 < x < 8)$ during the Li storage process.[8–10]

In order to combat these drawbacks and improve the electrochemical properties of MoS_2, a variety of methods have been explored, such as integrating MoS_2 with some high conductive materials or expanding the interlayer distance of MoS_2. Integrating nanosized MoS_2 with RGO to form MoS_2/RGO composite is one of the most effective strategies to improve the electrochemical performance of MoS_2.[11] RGO has high specific surface area and flexible structure, and it can improve the electric conductivity of MoS_2 remarkably and thus effectively enhance the electrochemical stability. At the same time, MoS_2 is RGO analogue which is in favor of combination with each other; thus, MoS_2 is more likely to grow on the surface of RGO. The monolayer nature of MoS_2 will maximize the available surface area and provide a maximum insertion active sites per unit area, which can enhance the ion adsorption on the surface.[12] In the previous studies, most of the MoS_2/RGO composites were prepared by hydrothermal or solvothermal methods at a temperature below 240°C due to the limitation of the Teflon liner.[13–15] Normally, the routine hydrothermal process need another subsequent calcination step at a temperature more than 500°C in order to obtain the composite with pure phase and prominent electrochemical properties, increasing the complication of the preparation process. Furthermore, few details in the literatures can be found on the one-pot preparation of mono- or bilayer of MoS_2 by a facile solvothermal process with temperature higher than 250°C.

In this work, we report a one-step high-temperature solvothermal approach (up to 350°C) to the preparation of MoS_2/RGO composite. Monolayer or bilayer of MoS_2 anchored onto RGO sheets (denoted as MoS_2/RGO composite) has been prepared and no exfoliation procedure and the subsequent calcination process are needed. The unique monolayer nanostructure can maximize the available surface area and provide more active sites per unit area for reaction with Li^+, which will be favorable for improving the electrochemical performance as an electrode material for LIBs and so on.

2. Experimental Section

2.1. *Materials*

Sodium molybdate dehydrate, thiourea and ethylene glycol were of AR grade and used as received without further purification. Graphene oxide (GO) powder, kindly provided by the Sixth Element (Changzhou) Ltd, was sonicated for 2 h before using. Pristine MoS_2 used as control sample was purchased from Shanghai Aladdin Bio-Chem Technology Co., LTD, and was used as received without further treatment.

2.2. *Synthesis of MoS_2/RGO composites*

The MoS_2/RGO composite nanosheets were prepared by a simple one-step solvothermal method. Sodium molybdate dihydrate ($Na_2MoO_4 \cdot 2H_2O$, 0.2 g) and thiourea (0.26 g) was dissolved in 5 mL ethylene glycol, and then 0.013 g graphene oxide was added to the mixture after stirring for 20 min. The suspension was sonicated at room temperature for about 2 h and then transferred into a Swagelok structured stainless autoclave with a capacity of 8 mL (a homemade stainless steel (316) high-pressure cell with a Swagelok fitting was used to maintain the pressure at high temperatures up to 400°C for H_2O). And then the autoclave was placed in a thermostatic oven and heated to 350°C and maintained at this temperature for 16 h. The autoclave was naturally cooled down to room temperature, and then the resultant black precipitate was collected centrifugally and washed three times with ultra-pure water and ethanol, respectively. The black product composed of MoS_2 and RGO was named as MoS_2/RGO and was then dried at 60°C in a thermostatic oven for 12 h.

2.3. *Characterization*

The crystallographic information and composition of the products were investigated by using a Rigaku

Ultima IV X-ray diffractometer (XRD, Cu-Kα radiation $\lambda = 0.15418$ nm). Raman spectra were collected using a Renishaw in Via Plus Micro-Raman spectroscopy system equipped with a 50 mW DPSS laser at 532 nm. The thermogravimetric analysis (TGA) was performed with a Mettler Toledo TGA-2 thermal gravimetric analyzer under an oxygen atmosphere with a heating rate of 10°C min^{-1}. The morphologies and the structures of the samples were examined by a JEOL JSM-7800F scanning electron microscope (SEM) equipped with an energy dispersive X-ray (EDX) and a JEOL JEM-2100Plus transmission electron microscope (TEM).

2.4. *Electrochemical testing*

The working electrodes were prepared by a simple slurry coating method; the slurry was made by mixing the active materials (MoS_2), acetylene black (super-P) and polyvinylidene fluoride (PVDF) in N-methyl-2-pyrrolidinone (NMP, Sigma Aldrich) with a weight ratio of 80:10:10, and then grinding for a period of time to obtain a heterogeneous mixture slurry. The slurry was subsequently cast on a copper foil, followed by drying in a vacuum oven at 110°C for 10 h to remove the solvent completely. The active materials loaded on the working electrode were controlled in the range of 1.45–1.65 mg · cm^{-2}. The CR2016 coin-type cells were then assembled in an argon-filled glove box. Celgard 2400 film, 1 molL^{-1} $LiPF_6$ and lithium metal foil were used as separator, electrolyte and counter electrode, respectively. The galvanostatic charge-discharge tests were carried out on a LAND Cell Test System (2001 A, Wuhan, China) with a voltage range of 0.01–3 V at different current densities. Cyclic voltammetry (CV) measurements were conducted at a scan rate 0.5 mV s^{-1} between 0.01 V and 3 V on a CHI760D electrochemical working station. The electrochemical impedance spectroscopy (EIS) tests were measured on a CHI760D electrochemical working station in a frequency range of 0.01 Hz to 100 kHz.

3. Results and Discussion

3.1. *Structure and morphology*

Figure 1(a) shows the XRD pattern of the MoS_2/RGO composite obtained by the one-step high-temperature solvothermal approach. In comparison to the characteristic XRD pattern of hexagonal MoS_2 (JCPDS 37-1492), the (002) reflection at ca. 14° and the (103) peak at about 39° disappear in the MoS_2/RGO composite, meanwhile the (110) reflection and the (110) peak shifted slight to the low angle direction, indicating the lack of structure perfection of the MoS_2 species in the MoS_2/RGO composite.[16] Actually, all these characteristics are consistent with the documented XRD pattern of single layer MoS_2.[17]

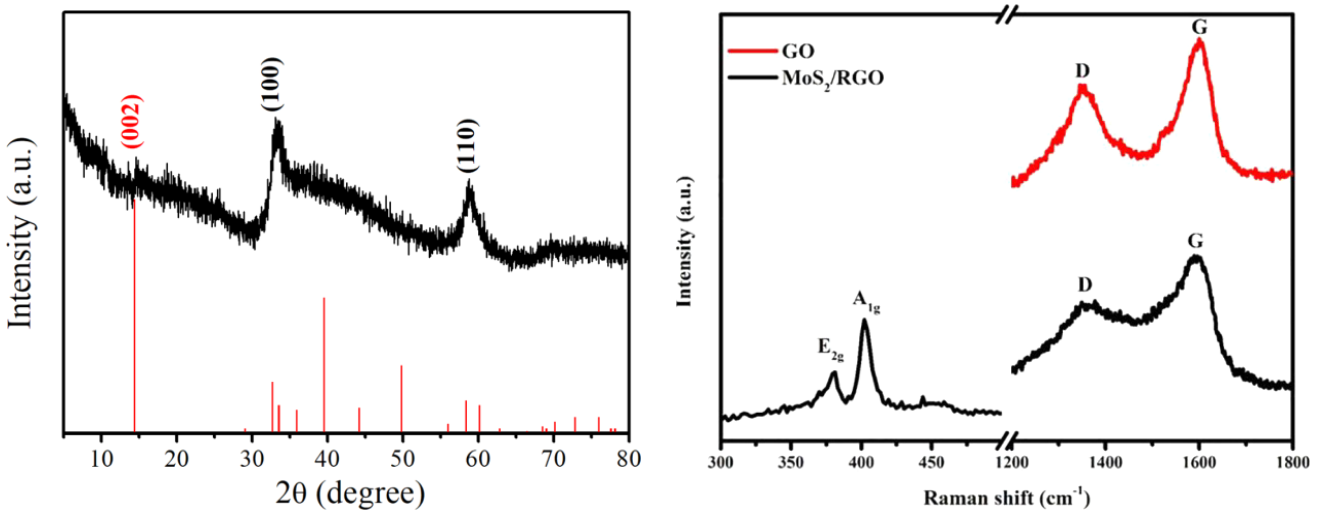

(a) (b)

Fig. 1. (a) XRD pattern and (b) Raman spectra of GO and MoS_2/RGO composite.

Figure 1(b) shows the Raman spectroscopy of the MoS_2/RGO composite. Two remarkable peaks centered at about 375 cm^{-1} (E_{2g}, corresponding to the in-plane displacement of Mo and S atoms) and 405 cm^{-1} (A_{1g}, corresponding to out-of-plane symmetric displacements of two S atoms along the c-axis).[18–20] Another two characteristic peaks located at around 1360 cm^{-1} (D, assigned to the vibrations of carbon atoms with dangling bonds for the in-plane terminations of disordered graphite) and 1590 cm^{-1} (G, assigned to the vibration of ordered sp^2 carbon atoms in a 2D hexagonal lattice) are attributed to carbon. The Raman spectroscopy illustrates the presence of carbon and MoS_2 in the composites. It is well-known that the ratio of peak intensity between bands D and G (I_D/I_G) is a critical parameter to estimate the degree of graphitization of carbon materials.[21] The calculated value of I_D/I_G for the MoS_2/RGO composite is 0.94, which is slightly higher than that of GO (0.83). Such a change may be caused by the anchoring of MoS_2 layers onto the RGO sheets and the existence of amorphous carbon introduced by carbonization of the ethylene glycol during the high temperature hydrothermal treatment.[22]

The morphologies of MoS_2/RGO composite were investigated using field-emission scanning electron microscopy (FESEM), and the corresponding images are shown in Fig. 2(a). A crumpled graphene framework can be seen and the crumpled RGO layers stack irregularly with many gaps in between. Figure 2(b) shows the EDX element mapping analysis, it can be seen that the composite contains mainly C, S and Mo elements dispersed well between RGO layers. Figure 2(c) shows the TEM image of the MoS_2/RGO composite, it can be seen

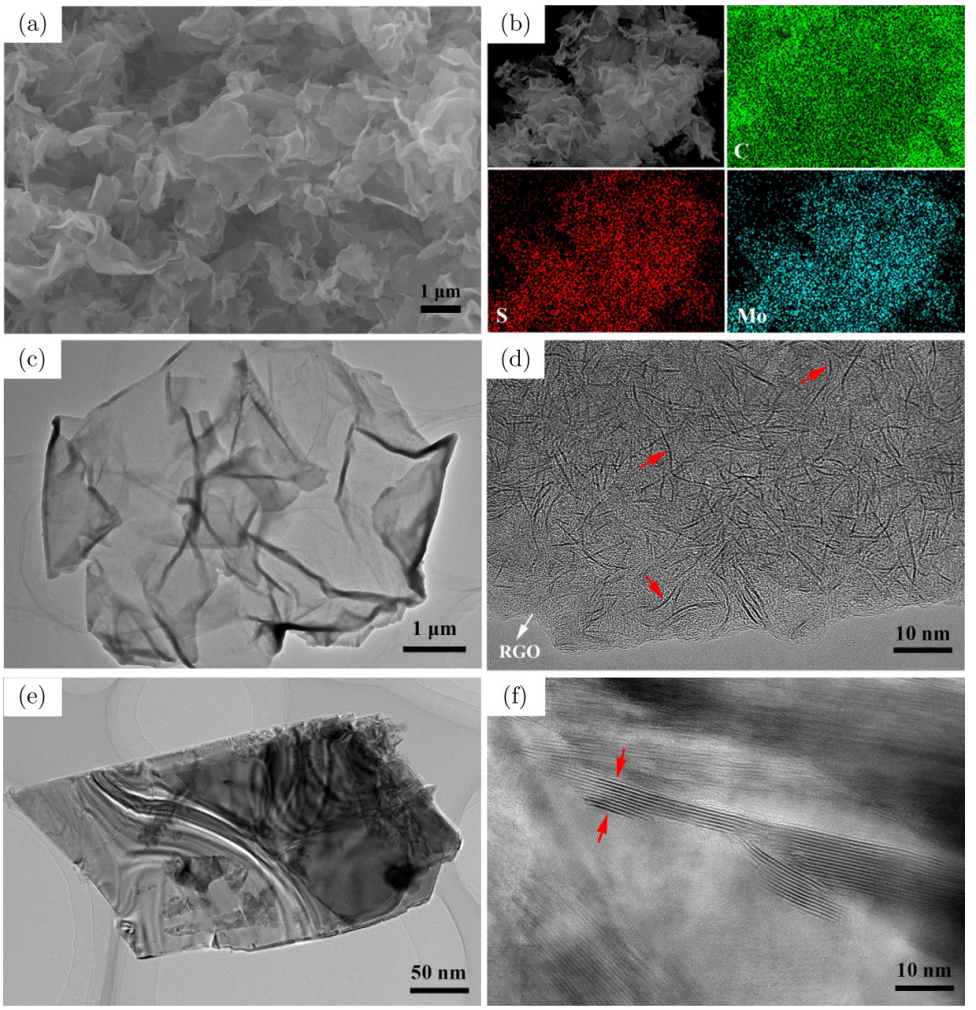

Fig. 2. SEM images (a), EDS mapping (b), TEM image (c) and HRTEM image (d) of the MoS_2/RGO composite, TEM image (e) and HRTEM image (f) of bare MoS_2.

that the surface of the crumpled RGO layers is roughly associated with the flexible and corrugated nature, which facilitated ionic conductivity inside the sample. From careful examination of the high-resolution TEM (HRTEM) image of Fig. 2(d), it can be clearly seen that a large number of randomly oriented monolayer MoS_2 (indicated by red arrows) distribute on the surface of the RGO layer, which is in good accordance with the XRD and Raman results. Figure 2(e) shows the TEM image of bare MoS_2, it can be seen that the sample is composed of stacking nanosheets. The HRTEM image as shown in Fig. 2(f) clearly exhibits the well-stacked structure of the MoS_2 nanosheets with about 11 layers.

To determine the amount of MoS_2 in the MoS_2/RGO composites, the TGA study was carried out. Figure 3 shows the TGA profile of MoS_2/RGO. The MoS_2/RGO composite was heated to 700°C in air, during which RGO and MoS_2 was oxidized to form gaseous species and MoO_3.[15,23] It can be seen that the composite shows a gentle weight loss below 200°C caused by the vaporization of adsorbed water and a significant weight loss between 300°C and 500°C, which was resulted from the oxidation of RGO, amorphous carbon and MoS_2. Based on the fact that the final product is MoO_3 after heating, it can be calculated that the mass fraction of MoS_2 in the MoS_2/RGO is about 59.4%.

3.2. *Electrochemical performance*

The electrochemical properties of MoS_2/RGO are investigated by CV measurement. Figure 4(a) shows the CV curve of the MoS_2/RGO composite for the first three cycles in the potential range of 0.01–3.0 V (versus Li/Li^+) at a scan rate of 0.5 mV s^{-1}. Three reduction peaks at 0.27 V, 0.6 V and 1.0 V are observed in the first cycle. The first reduction peak at 1.0 V owes to lithium insertion into the interlayer of MoS_2 to form Li_xMoS_2 as described in Eq. (1).[24–26] The reduction peaks at 0.6 V and 0.27 V correspond to the conversion reaction of Li_xMoS_2 to Li_2S and metallic Mo, accompanying the establishing of a solid electrolyte interphase (SEI) film as indicated with Eq. (2).[21,27–30] The CV curves at the second and third cycles are similar, which illustrates good reversibility of the MoS_2/RGO composite electrode.

$$MoS_2 + xLi^+ + xe^- \rightarrow Li_xMoS_2, \quad (1)$$

$$Li_xMoS_2 + (4-x)Li^+ + (4-x)e^- \rightarrow Mo + Li_2S. \quad (2)$$

Figure 4(b) shows the charge-discharge curves of the MoS_2/RGO composite at the current density of 200 mA g^{-1} in the voltage range of 0.005–3 V, which are in good accordance with the previous CV results. For example, one plateau at approximately 0.6 V in the first discharge process is observed, which corresponds to the reduction peak at 0.67 V in the first CV curve [Fig. 4(a)]. Meanwhile, another two plateaus at approximately 0.3 V and 1.1 V in the first discharge process are not obvious, which are accord with the reduction peak at 0.27 V and 1 V in the first CV curve, respectively. The sloping curve of the MoS_2/RGO composite below 0.7 V could be attributed to the formation of the SEI film and the irreversible reaction between Mo and Li_2S.[30,31] In the subsequent discharge curves, the plateaus showed in the first curve disappears but two new plateaus at around 2.0 V and 1.3 V emerged, which is in agreement with the lithiation processes.

The cycle performances of the MoS_2/RGO composite and bare MoS_2 powder electrodes at a current density of 200 mA g^{-1} are shown in Fig. 4(c), together with the Coulombic efficiency of MoS_2/RGO composite. It can be found that the capacity of the MoS_2/RGO composite electrode illustrates a rising process in the first 8 cycles because of the gradual activation of the MoS_2/RGO composite before reaching its maximum reversible capacity.[22] In the subsequent 12 cycles, the reversible capacity decreased due to the slight stacking/restacking of monolayer MoS_2 into few layers during

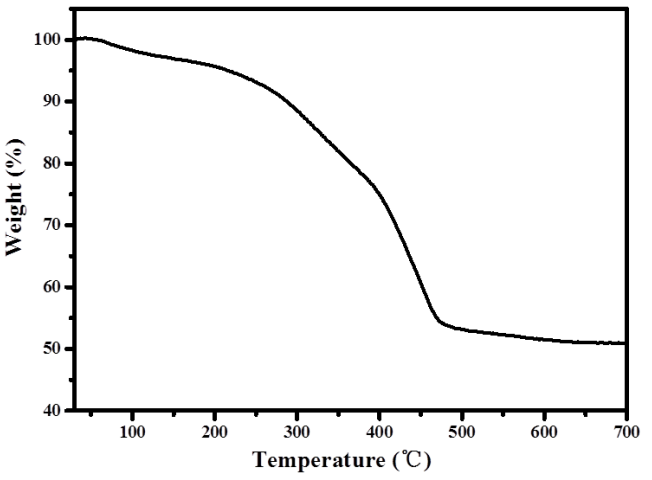

Fig. 3. TGA curves of MoS_2/RGO composite.

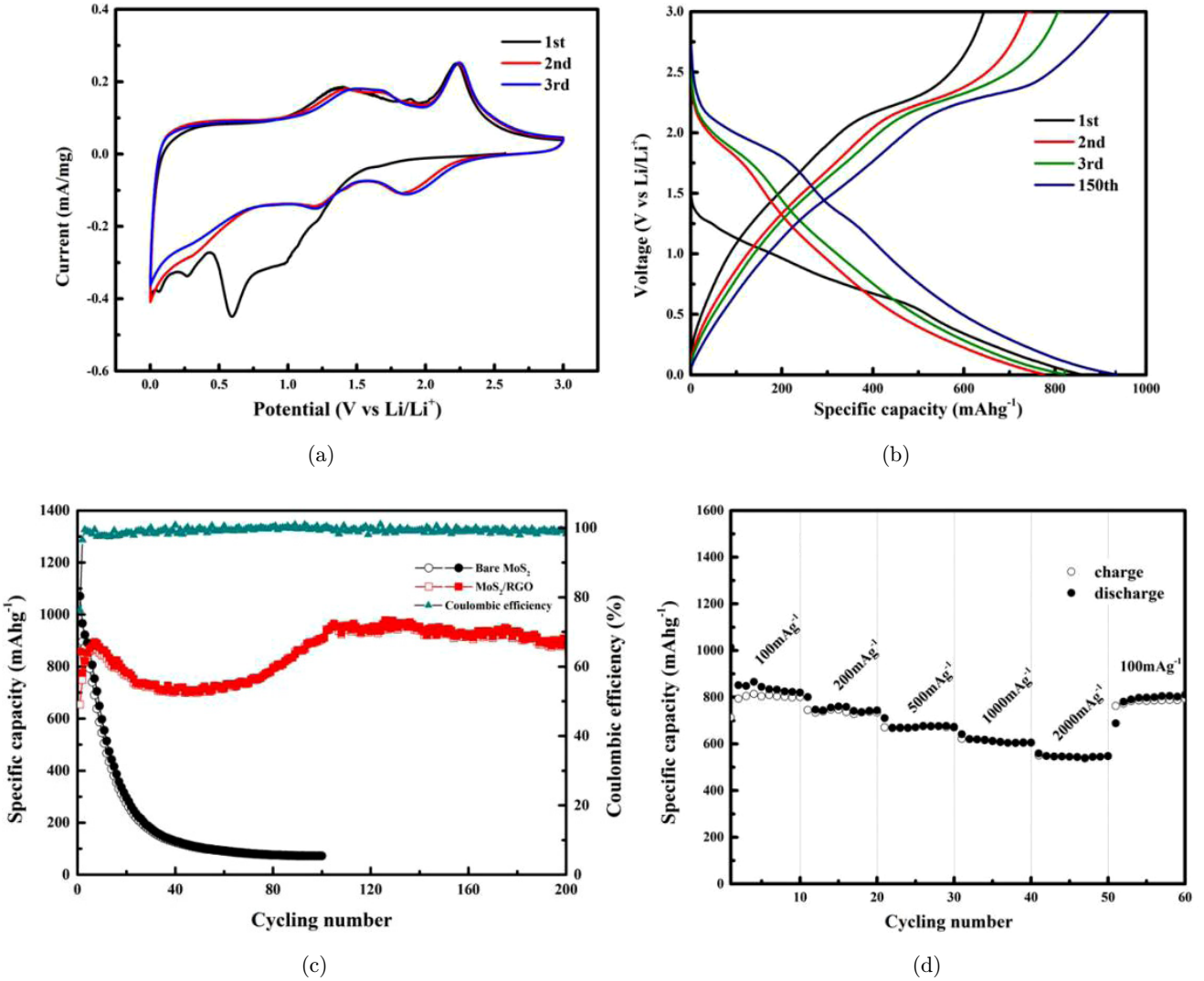

Fig. 4. The electrochemical performances of the MoS_2/RGO composite electrode. CV curves at a scan rate of 0.5 mV s^{-1} for the initial 3 cycles (a), charge–discharge voltage profiles at a current density of 500 mA g^{-1} (b), charge-discharge cycling results of MoS_2/RGO and bare MoS_2 powder at a current density of 500 mA g^{-1} (c), and rate performance at various current densities from 100 mA g^{-1} to 2000 mA g^{-1} (d).

charge/discharge process. After the preliminary 20 cycles, the reversible capacity demonstrates a gradual rising trend, which was attributed to the gradual introduction of new microchannels with repeated lithium ion insertion/extraction.[11] After 200 cycles, the capacity of the electrode stabilized at approximately 900 mAh g^{-1} with a Coulombic efficiency of 98%. While the bare MoS_2 electrode only retained 72 mAh g^{-1} after 100 cycles, probably due to the deconstruction and restacking of MoS_2. The superior cycling performance of the MoS_2/RGO composite electrode is attributed to the monolayer structure of MoS_2, which can maximize the available surface area and provide a maximum insertion active sites per unit area during the electrochemical cycling.[12] Meanwhile, the crumpled RGO and amorphous carbon relieve the volume change of MoS_2 keeping the stability of its structure during cycling.[32] To investigate the high-rate capability of the MoS_2/RGO composite electrodes, a multiple current galvanostatic testing has been conducted as shown in Fig. 4(d). The electrode delivered reversible capacities of about 950, 880, 800, 720 and 670 mA g^{-1} at 0.1, 0.2, 0.5, 1 and 2 A g^{-1}, respectively. When the current density was brought back to 100 mA g^{-1}, the reversible capacity returns to the original value 1000 mAh g^{-1} illustrating no prominent capacity decline after cycling under high

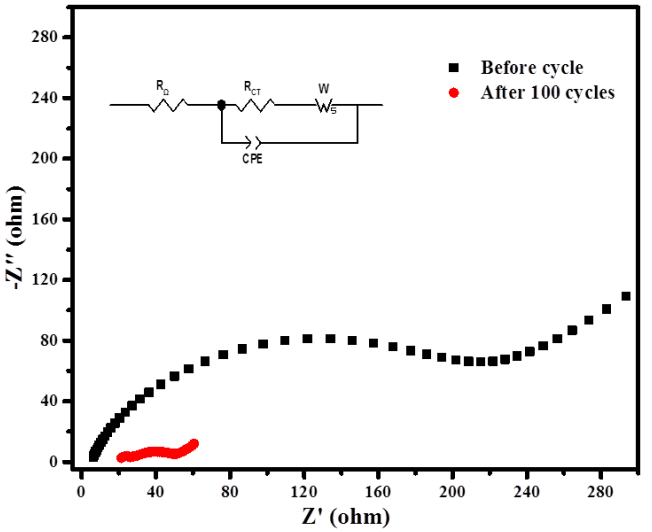

Fig. 5. (a) EIS curves of the MoS_2/RGO composite before cycling and after 100 cycles and the equivalent circuit in the inset.

current densities, which demonstrates the stable nanostructure of the MoS_2/RGO composite during the cycle.

To further confirm the excellent electrochemical performance of the MoS_2/RGO composite electrode, EIS is measured. Figure 5 shows the EIS spectra of the MoS_2/RGO composite before and after 100 cycles. The two impedance spectra consist of semicircles at high and medium frequencies and linear tail at low frequency. The semicircles at high frequency are assigned to the SEI resistance (R_{SEI}) and contact resistance (R_f). The semicircles at medium frequency are indicative of the charge-transfer resistance (R_{ct}). The linear tails at low frequency associates with the Warburg impedance (Z_w) corresponding to the diffusion of lithium ions into the bulk electrode.[33,34] It can be clearly seen that the diameter of the semicircles obtained after 100 cycles for the MoS_2/RGO composite electrode at high and medium frequencies are dramatically smaller than that before the cycling study, illustrating the introduction of new micro channels. This result demonstrates the increased capacity in the cycling stability test.

4. Conclusion

A composite consisting of monolayer or bilayer of MoS_2 deposited onto RGO sheets have been successfully fabricated via a facile one-pot high-temperature solvothermal approach (up to 350°C). The MoS_2/RGO composite electrode exhibits improved electrochemical performances including stable cycling performance, highly reversible specific capacity and enhanced good rate capability in a lithium-ion battery cell. The excellent electrochemical performance can be attributed to the disordering of the MoS_2 layers and the high conductivity of graphene, which are favorable for rapid ion and electron transport and electrolyte access during the electrochemical lithiation/delithiation process. These interesting properties make this material as eco-friendly and high-efficient anode material in lithium-ion battery. This high-temperature solvothermal method does not require post-calcination as in the routine solvothermal process, while it constitutes a new approach to the preparation of MoS_2 in mono- or bilayer. Further development of this method may make MoS_2 monolayer or bilayer useful as a high surface area species for integrated sensors or photocatalyst of high efficiency.

Acknowledgments

This work is supported by the Double First Class University Construction of Shandong Province, the Taishan Scholars Advantageous and Distinctive Discipline Program of Shandong Province for supporting the research team of energy storage materials, and Qingdao Basic & Applied Research Project (15-9-1-56-jch). Y. Q. Wang thanks the financial support from the Top-notch Innovative Talent Program of Qingdao City (Grant no.: 13-CX-8).

References

1. J. M. Tarascon and M. Armand, *Nature* **414**, 359 (2001).
2. X. W. Liu, X. H. Liu, B. F. Sun, H. L. Zhou, A. P. Fu, Y. Q. Wang, Y.-G. Guo, P. Z. Guo and H. L. Li, *Carbon* **130**, 680 (2018).
3. B. Dunn, H. Kamath and J. M. Tarascon, *Science* **334**, 928 (2011).
4. N. Ma, X. H. Liu, Z. Yang, G. Tai, Y. Yin, S. B. Liu, H. L. Li, P. Z. Guo and X. S. Zhao, *ACS Sustain. Chem. Eng.* **6**, 1133 (2018).
5. N. M. Choi, Z. Chen, S. A. Freunberger, X. Ji, Y. K. Sun, K. Amine, G. Yushin, L. F. Nazar, J. Cho and P. G. Bruce, *Angew. Chem. Int. Ed.* **51**, 9994 (2012).
6. D. D. Liu, Z. Kong, X. H. Liu, A. P. Fu, Y. Q. Wang, Y. G. Guo, P. Z. Guo, H. L. Li and X. S. Zhao, *ACS Appl. Mater. Interfaces* **10**, 2515 (2018).

7. J. B. Goodenough and Y. Kim, *Chem. Mater.* **22**, 587 (2010).
8. J. M. Jeong, K. G. Lee, S. J. Chang, J. W. Kim, Y. K. Han, S. J. Lee and B. G. Choi, *Nanoscale* **7**, 324 (2015).
9. S. B. Yang, X. L. Feng, L. Wang, K. Tang, J. Maier and K. Müllen, *Angew. Chem. Int. Ed.* **49**, 4795 (2010).
10. J. Xiao, X. Wang, X. Q. Yang, S. Xun, G. Liu, P. K. Koech, J. Liu and J. P. Lemmon, *Adv. Funct. Mater.* **21**, 2840 (2011).
11. Y. F. Chao, R. Jalili, Y. Ge, C. Y. Wang, T. Zheng, K. W. Shu and G. G. Wallace, *Adv. Funct. Mater.* **27**, 1700234 (2017).
12. N. Savjani, E. A. Lewis, Mark A. Bissett, Jack R. Brent, Robert A. W. Dryfe, S. J. Haigh and P. O'Brien, *Chem. Mater.* **28**, 657 (2016).
13. L. Y. Jing, A. P. Fu, H. L. Li, J. Q. Liu, P. Z. Guo, Y. Q. Wang and X. S. Zhao, *RSC Adv.* **4**, 59981 (2014).
14. Y. J. Gong, S. B. Yang, L. Zhan, L. L. Ma, R. Vajtai and P. M. Ajayan, *Adv. Funct. Mater.* **24**, 125 (2014).
15. L. Ma, G. C. Huang, W. X. Chen, Z. Wang, J. B. Ye, H. Y. Li, D. Y. Chen and J. Y. Lee, *J. Power Sources* **264**, 262 (2014).
16. H. S. S. R. Matte, A. Gomathi, A. K. Manna, D. J. Late, R. Datta, S. K. Pati and C. N. R. Rao, *Angew. Chem. Int. Ed.* **49**, 4059 (2010).
17. P. Joensen, R. F. Frindt and S. Roy Morrison, *Mater. Res. Bull.* **21**, 457 (1986).
18. J. Zhang, H. Yu, W. Chen, X. Z. Tian, D. H. Liu, M. Cheng, G. B. Xie, W. Yang, R. Yang and X. D. Bai, *ACS Nano* **8**, 6024 (2014).
19. X. S. Wang, H. B. Feng, Y. M. Wu and L. Y. Jiao, *J. Am. Chem. Soc.* **135**, 5304 (2013).
20. I. Song, C. Park, M. Hong, J. Baik, H. J. Shin and H. C. Choi, *Angew. Chem. Int. Ed.* **126**, 1290 (2014).
21. M. Sevilla and A. B. Fuertes, *ACS Nano* **8**, 5069 (2014).
22. S. Tyler, Z. Li, B. Olsen and D. Mitlin, *Energy Environ. Sci.* **7**, 209 (2014).
23. J. E. Liu, A. P. Fu, Y. Q. Wang, P. Z. Guo, H. B. Feng, H. L. Li and X. S. Zhao, *ChemElectroChem* **4**, 2027 (2017).
24. J. Xiao, D. Choi, L. Cosimbescu, P. Koech, J. Liu and J. P. Lemmon, *Chem. Mater.* **22**, 4522 (2010).
25. G. Du, Z. Guo, S. Wang, R. Zeng, Z. Chen and H. Liu, *Chem. Commun.* **46**, 1106 (2010).
26. L. David, R. Bhandavat and G. Singh, *ACS Nano* **8**, 1759 (2014).
27. B. H. Xu, X. G. Guan, L. Y. Zhang, X. W. Liu, Z. B. Jiao, X. H. Liu, X. Q. Hu and X. S. Zhao, *J. Mater. Chem. A* **6**, 4048 (2018).
28. H. L. Zhou, D. X. Wang, A. P. Fu, X. H. Liu, Y. Q. Wang, Y. H. Li, P. Z. Guo, H. L. Li and X. S. Zhao, *Mater. Sci. Eng. B* **227**, 9 (2018).
29. K. Chang and W. X. Chen, *ACS Nano* **5**, 4720 (2011).
30. Y. Liu, Y. Zhao, L. Jiao and J. Chen, *J. Mater. Chem. A* **2**, 13109 (2014).
31. X. M. Zhou, P. Gao, S. C. Sun, D. Bao, Y. Wang, X. B. Li, T. T. Wu, Y. J. Chen and P. P. Yang, *Chem. Mater.* **27**, 6730 (2015).
32. N. Savjani, E. A. Lewis, M. A. Bissett, J. R. Brent, R. A. W. Dryfe, S. J. Haigh and P. O'Brien, *Chem. Mater.* **28**, 657 (2016).
33. D. X. Wang, A. P. Fu, H. L. Li, Y. Q. Wang, J. Q. Liu, P. Z. Guo and X. S. Zhao, *J. Power Sources* **285**, 469 (2015).
34. J. W. Zhou, J. Qin, X. Zhang, C. S. Shi, E. Z. Liu, J. J. Li, N. Q. Zhao and C. N. He, *ACS Nano* **9**, 3837 (2015).